

Effect of Tempering Time on Corrosion Resistance of High Co-Ni Steel

Xin-yuan Wang¹, Xin-yi Liu², Chen-chong Wang³, Tian-xiang Li¹, Duo Liu⁴, Xu Wang^{1,*},
Jian-min Ren^{1,*}, J.C. Huang⁵

¹ School of Mechanical Engineering, Liaoning Petrochemical University, Fushun 113001, Liaoning, China

² College of Pipeline and Civil Engineering, China University of Petroleum, Qingdao, 266555 Shandong, China

³ State Key Laboratory of Rolling and Automation, School of Materials Science and Engineering, Northeastern University, Shenyang, 110819, Liaoning, China

⁴ Shenyang Institute of Special Equipment Inspection and Research, Shenyang, 110065, Liaoning, China

⁵ Department of Materials Science and Engineering, Hong Kong Institute for Advanced Study, City University of Hong Kong, Kowloon, Hong Kong

*E-mail: wx1979875@hotmail.com, Jmren661216@163.com

Received: 15 September 2022 / *Accepted:* 26 October 2022 / *Published:* 17 November 2022

The present study attempts to improve corrosion resistant of high Co-Ni steel in ~ 1.0 wt% NaCl environment at 25 °C (room temperature) by different tempering times. Microstructures of specimens were characterized by X-ray diffraction (XRD), and scanning electron microscopy (SEM). The corrosion behavior was evaluated by polarization curve and electrochemical impedance spectroscopy. Firstly, the tempering time has a great influence on the morphology of martensite lath in high Co-Ni steel. Secondly, it was observed from the experimental data that a passivation/oxide layer with N-type semiconductor behavior was formed on all the samples studied in this paper. Increasing the tempering time can move the corrosion potential forward. Finally, tempering time of 16 h effectively improves the overall stability of the sample surface and reduces the corrosion tendency of the sample.

Keywords: High Co-Ni steel, Tempering temperatures, Corrosion behavior, Microstructure, Electrochemical corrosion

1. INTRODUCTION

Some current applications of high Co-Ni steel are aerospace, equipment manufacturing, transportation, petroleum and petrochemical equipment. It has many advantages such as high strength

and toughness, good wear resistance and corrosion resistance [1-4]. At present, it has been successfully used in important transmission components such as the main rotor shaft and transmission shaft of the Osprey, Bell, and CH-47 helicopters. With the continuous expansion of market demand for special gear steel, high Co-Ni steel has become a common material for special gear steel.

The lath martensite is obtained by quenching usually has higher strength and lower toughness, so tempering is a necessary procedure to improve its toughness [5-7]. Various carbides precipitate at different tempering temperatures, so the tempering temperature has a significant effect on the corrosion resistance of the steel. In the past, much work has been done on how tempering temperatures affect the corrosion resistance of steels [8-12]. However, they pay little attention to the effect of tempering time on corrosion resistance. Feng Yuan et al. [13] found that controlling corrosion of Cr-13 martensitic stainless steel by changing tempering time.

In this study, the microstructures, corrosion behaviors, as well as corrosion mechanisms are carefully investigated. High Co-Ni steel is tempered at 482 °C for different time. The microstructure evolution of high Co-Ni steel is characterized by scanning electron microscopy (SEM). The corrosion resistance of gear steel with different tempering time in corrosive medium is studied by polarization and EIS in 1.0 wt % NaCl solution. At the same time, the corrosion mechanism of high Co-Ni steel with high corrosion resistance is discussed by changing the tempering time. It provides a reference for optimizing the heat treatment process of high Co-Ni steel.

2. EXPERIMENTAL

2.1 Materials

The experimental samples were melted and forged into 53 mm thick bars by vacuum induction + vacuum consumption (VIM+VAR), and then 4 mm thick high Co-Ni steel was obtained by 8 passes hot rolling. The chemical composition of steel produced in the laboratory is shown in Table 1.

Table 1 Chemical compositions of the high Co-Ni steel (wt.%)

Compositions	Co	Ni	Cr	Mo	V	C	Fe
Content	12.20	7.60	3.58	0.96	0.023	0.16	Bal.

2.2 Heat treatment

According to the reference provided by JMatPro material performance calculation software for the heat treatment temperature of the sample, the heat treatment process is as follows: austenitizing at 950 °C for 1h, then water quenching, cold treatment at -73 °C for 1 h, and finally holding at 482 °C for 8 h, 12 h, 16 h, and 20 h respectively. Heat treatment process is shown in Figure 1.

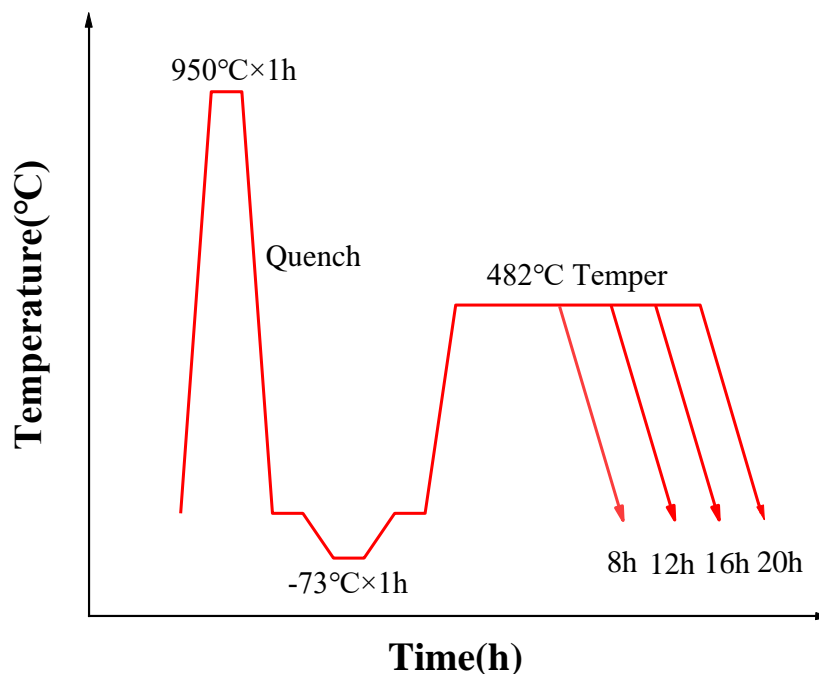


Figure 1. Heat treatment process

2.3 Microstructure characterization

The X-ray diffraction (XRD) analysis of the experimental steel was carried out by using Cu K α radiation on the D8 advance X-ray diffractometer. A mode with a 2θ range ($20-90^\circ$) is used to analyze the main structure of each sample, while a mode with $0.02^\circ/\text{step}$ is used to obtain the detailed information in each heat treatment sample. The average hardness value of the tested steel was obtained by using LGTHVS-3A Vickers microhardness tester at least 5 repeated test points on each sample. All samples were corroded with 4% nitric acid alcohol and their surface morphology was observed by TESCAN VEGA II LMU scanning electron microscope (SEM).

2.4 Electrochemical test process

Electrochemical tests were performed using an electrochemical workstation (CS350, CorrTest). Electrochemical tests the corrosion resistance of the specimens was tested using a three-electrode system. In electrochemical tests, platinum electrode was used as auxiliary electrode, saturated calomel electrode (SCE) as reference electrode, and sample as working electrode. For each sample, a newly configured 500 ml 1.0 wt. % NaCl solution was used, and water bath heating was used to ensure that the ambient temperature was $25 \pm 0.5^\circ\text{C}$.

Potentiodynamic polarization scans were made with scan rate of 1 mV/s and a scanning range of -0.3 V to 1 V vs OCP. Each sample was tested at least three times to ensure reproducibility and accuracy of the data. Potentiodynamic polarization data were fitted and analyzed using the software CorrTest CS Studio attached to the electrochemical workstation. EIS test was also performed at $25 \pm 0.5^\circ\text{C}$ in 1.0 wt. % NaCl solution at room temperature. EIS test potential selection frequency range is 0.01Hz~100kHz. The impedance spectrum was recorded using a sinusoidal potential signal with an amplitude of 10 mV, and a logarithmic scan was performed every 10 points. The impedance spectrum

was fitted with ZSimpWin data fitting software. The M-S curves of samples with different tempering time were tested at 1 kHz.

3. RESULTS AND DISCUSSION

3.1 Microstructure characterization

The surface microstructure of the samples with different tempering time is shown in Figure 2. The microstructures of the specimens with different tempering time are lath martensite, retained austenite and a small amount of carbide. For samples with different tempering time, lath martensitic has obvious characteristics. When the tempering time is short, in Figure 2 (a) (b), the original austenite grain boundary is clear and the martensite lath is small. When the tempering time is 16 h (Figure 2 (c)), the fine insoluble phase is dispersed in the martensite matrix, and the size of lath martensite is uniform. When the tempering time continues to increase to 20 h (Figure 2 (d)), the martensite lath begins to grow and become longer, the lath martensite structure gradually disappears, and more fine particles precipitate in the matrix. As Wang et al. [14] found that the tempering process also affects the grain size. Of course, the lower the tempering temperature and the shorter the time, the smaller the grain size of martensite matrix.

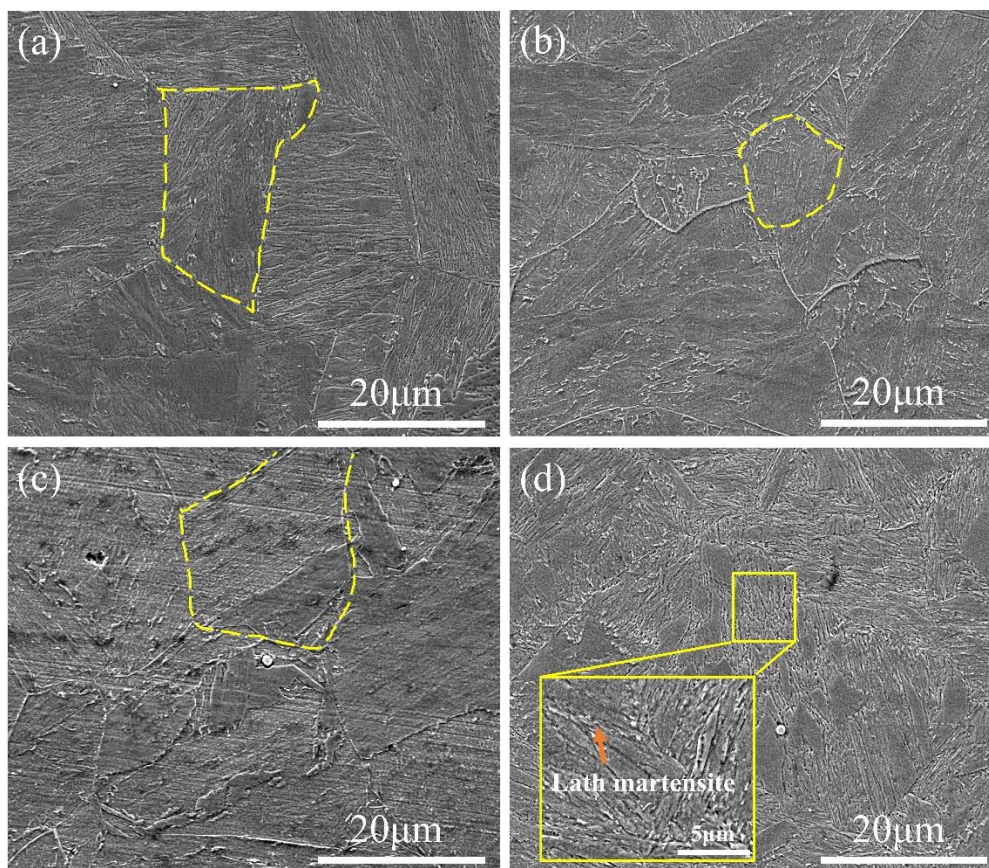


Figure 2. Metallography of the high Co-Ni steel with different tempering time (a) 8 h, (b) 12 h, (c) 16 h, (d) 20 h

In order to further confirm the phase and structure, we carried out XRD analysis. The XRD spectrum of the sample is shown in Figure 3. It can be seen that there are obvious diffraction peaks at about 45° , 65° and 82° . However, it is found by fitting with Jade software that 2θ may have different peaks of face-centered $M_{23}C_6$ carbides in the range of 47° - 52° . Pandey et al. [15] found that the coarsening of secondary phase carbide particles $M_{23}C_6$ was revealed with an increase in tempering time. As Figure 2, the size of carbide increases with the increase of tempering temperature. In the process of carbide growth, in addition to changes in size and composition, structural changes may also occur. If the carbide structure changes, its stability is worse, and it is not conducive to the maintenance of hardness.

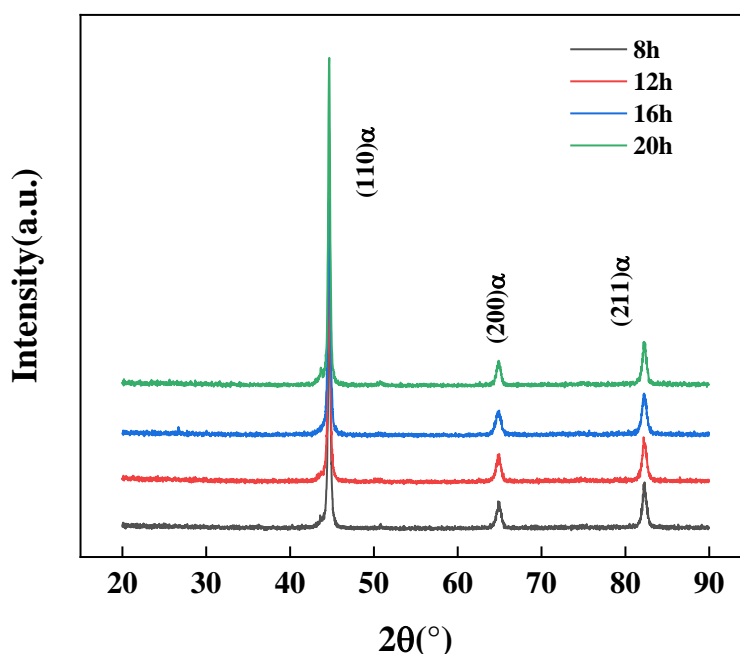


Figure 3. XRD patterns of the high Co-Ni steel with different tempering time

By comparing the hardness (Figure 4), it is found that the hardness of high Co-Ni steel decreases with increasing tempering time. The hardness of high Co-Ni steel tempered for 8-20 h ranges from 420 to 377 HV. The hardness decreases slightly with the increase of tempering time, indicating that the tempering time has little effect on the hardness. The reason for the hardness decrease may be that the internal stress is released with the increase of tempering time, and the martensite morphology changes. The lath martensite appears and becomes wider. It is also possible that the carbide size has changed. The hardness decreases slowly after the tempering time is extended for 16 h, which indicates that the cementite particles with smaller size can also pin roll dislocations, hinder the migration of grain boundaries, and hinder the recovery of martensite, thus slowing down the hardness reduction caused by the recovery of the matrix [16].

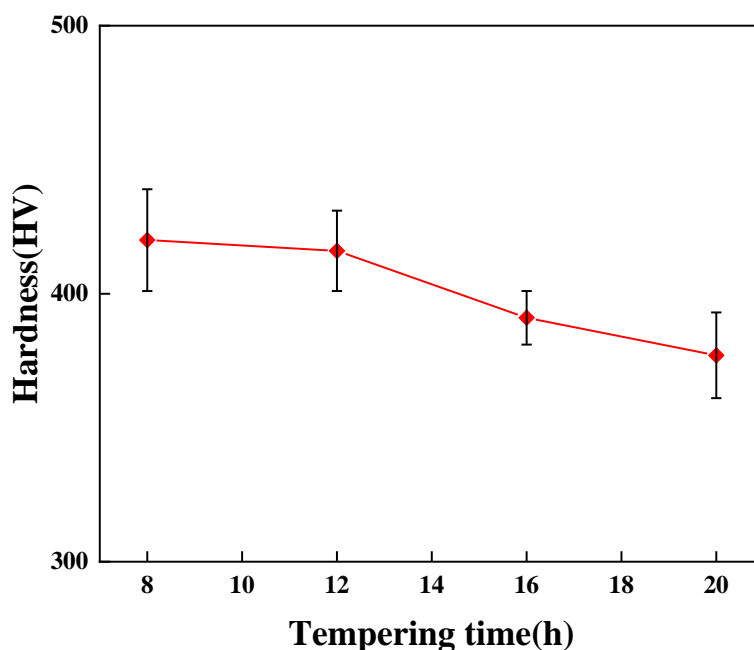


Figure 4. The hardness of the high Co-Ni steel with different tempering time

3.2 Potentiodynamic polarization tests of the high Co-Ni steel

Figure 5 shown the potentiodynamic polarization curves of the high Co-Ni steel with different tempering time, and clearly describes the influence of corrosion solution on the corrosion tendency and corrosion rate of the test steel. To study the effect of different tempering time on the corrosion resistance of tested steel, polarization tests were carried out for four tempering time. All the tested samples were tested for OCP in 1.0 wt. % NaCl solution at 25 °C for 1 h to ensure the accuracy and stability of the experiment. From the polarization curve, the order of positive corrosion potential (E_{corr}) is: 16 h > 20 h > 12 h > 8 h.

Table 2 is the fitting data of potentiodynamic polarization curve. The fitting data also proves that it conforms to the trend of potentiodynamic polarization curve ($E_{16h} = -0.189 V_{SCE} > E_{20h} = -0.259 V_{SCE} > E_{12h} = -0.304 V_{SCE} > E_{8h} = -0.414 V_{SCE}$). However, the corrosion current density (I_{corr}) decreases according to the law of 16 h < 20 h < 12 h < 8 h ($I_{8h} = 4.191 \times 10^{-6} > I_{12h} = 1.154 \times 10^{-7} > I_{20h} = 9.622 \times 10^{-8} > I_{16h} = 2.701 \times 10^{-8}$). With the increase of tempering time, the corrosion density (I_{corr}) changes obviously. The trend of corrosion current density and corrosion potential was consistent, which indicated that the specimen with the tempering time of 16 h had excellent corrosion resistance. It is worth noting that except for the samples tempered for 8 h, the other three groups all have a temporary passivation zone, which indicates that corrosion products have been formed during the dissolution of the matrix, leading to surface passivation, which will play a temporary role in protecting the surface of the sample. When a protective film is formed on the surface of the sample, Cl^- will accumulate at the interface of the protective film, contacting the metal surface sufficiently to accelerate corrosion. The corrosion of the sample in NaCl solution is accomplished by electron transfer, which is actually anodic dissolution and cathodic reduction [17]. When the tempering time reaches 16 h, the grain of the sample is finer, and

these fine grains are beneficial to produce a dense oxide film and passivation film on the surface of the sample.

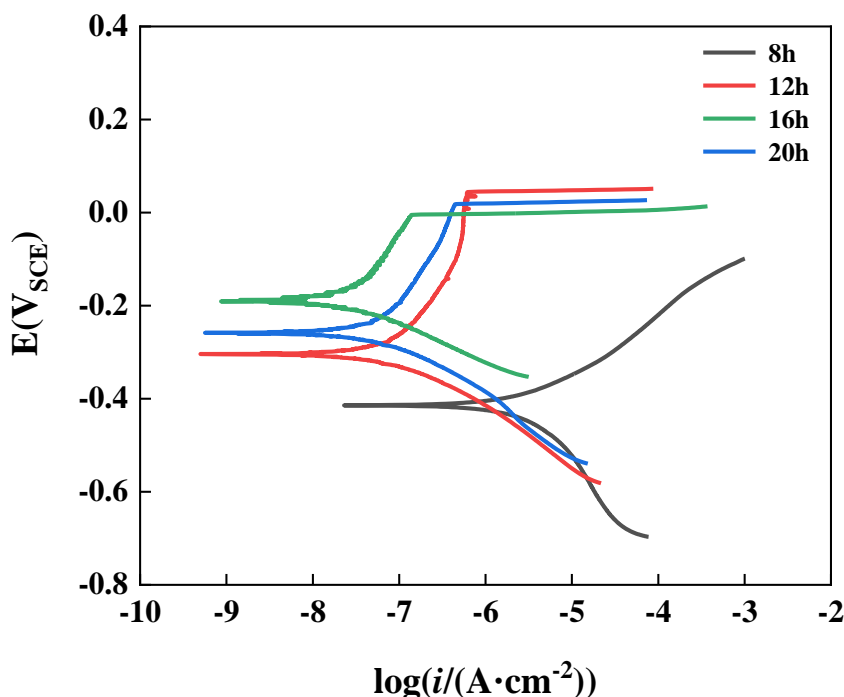


Figure 5. Potentiodynamic polarization curve of the high Co-Ni steel in 1.0 wt.% NaCl solution (Tempering time: 8 h, 12 h, 16 h and 20 h)

Table 2 Potentiodynamic polarization curve fitting data of the tempering time in 1.0 wt.% NaCl solution

Tempering time (h)	Corrosion potential (V_{SCE})	Corrosion current density (A/cm^2)
8	-0.414	4.191×10^{-6}
12	-0.304	1.154×10^{-7}
16	-0.189	2.701×10^{-8}
20	-0.259	9.622×10^{-8}

3.3 EIS of the high Co-Ni steel

To further investigate the effect of oxide layer/passivation layer on the corrosion behavior of different samples, we conducted an impedance test in 1.0 wt. % NaCl solution at 25 °C. Figure 6 (a) (b) shows the bode spectra of samples with different tempering time. Figure 6 (c) shows the equivalent circuit. In the equivalent circuit diagram, the solution resistance (R_s) is connected in series with the

constant phase element (CPE), and the CPE is connected in parallel with the charge transfer resistance (R_{ct}). From Figure 6 (a)(b) that the phase angle is close to 0° in the high frequency region, which indicates that the impedance in the high frequency region can be characterized by the resistance R_s . The phase angle variation of different tempering time in the intermediate frequency region at $60-80^\circ$ is related to the interface charge transfer of the space charge layer. The low frequency region is often considered as the transmission of defects in the passivation film, which can be characterized by R_{ct} . In the low frequency region, the phase angle of different tempering time are quite different [18-21].

All impedance spectra were fitted by ZsimpWin impedance fitting software. Table 3 shows the fitting results of bode curve [18,19]. The R_{ct} value is considered to be related to the composition and thickness of the passivation film. In the work, the R_{ct} value of the 16 h tempered sample is significantly larger than that of other tempered samples, which indicates that the experimental steel is more likely to form a denser passivation layer/oxide layer when the tempering time is 16 h, showing higher corrosion resistance than other samples. The conclusion of passivation layer/oxide layer thickness is further proved in the subsequent Mott- Schottky curve.

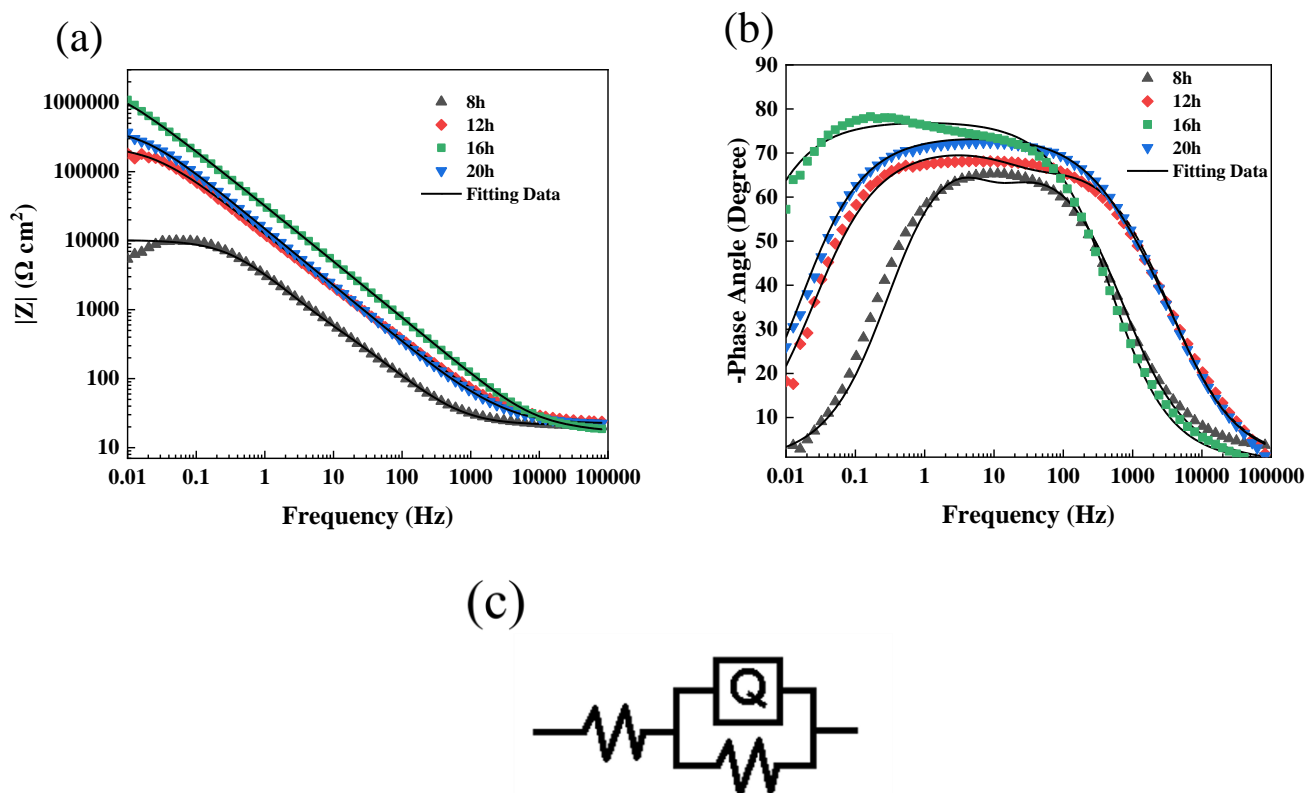


Figure 6. EIS spectra and fitting results of the high Co-Ni steel in 1.0 wt.% NaCl solution: (a)(b) Bode plots, (c)Electrical equivalent circuit (Tempering time: 8 h, 12 h, 16 h and 20 h)

Table 3. EIS fitting results were obtained using the equivalent circuit in Figure 6 (c)

Tempering time (h)	R_s ($\Omega \text{ cm}^2$)	$CPE_p \times 10^{-5}$ ($\Omega^{-1} \text{ cm}^{-2} \text{ S}^{-n}$)	n	R_{ct} ($\Omega \text{ cm}^2$)
8	20.99	6.34	0.79	1.07×10^4
12	23.82	1.85	0.78	2.56×10^5
16	31.55	3.17	0.86	1.31×10^6
20	22.96	1.49	0.82	4.50×10^5

3.4 Mott-Schottky test of the high Co-Ni steel

To characterize the semiconducting properties of the surface passivation/oxide layer of the samples with different tempering temperatures in this paper, Mott-Schottky tests were performed at 1 kHz in 1.0 wt. % NaCl solution at room temperature at 25 °C.

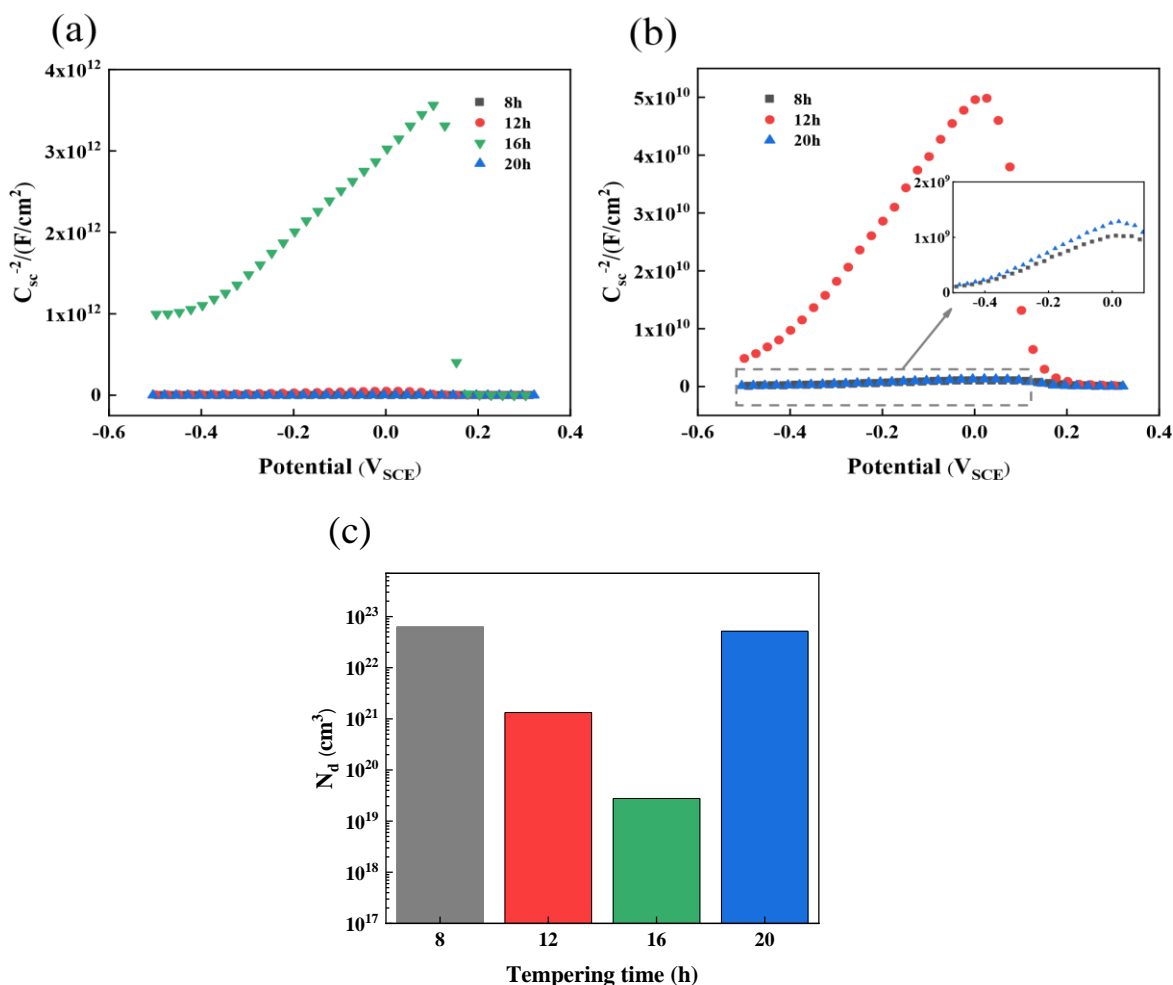


Figure 7. Mott-Schottky for different tempering time samples in 1.0 wt.% NaCl solution (a) M-S curve, (b) M-S curve enlarged view, (c) Main energy level density

The AC amplitude is 10 mV, the potential range is -0.5~0.75 VS OCP, and the potential increment is 0.025 V. Figure 7(a) shows the M-S of samples with different tempering times, and Figure 7(b) is the enlarged image of Figure 7(a). From the Mott-Schottky, it can be seen that the protective passivation/oxide layer on the surface of the sample has changed significantly after different tempering time.

According to Mott-Schottky theory, the space charge capacitance of N-type or P-type semiconductors can be calculated as follows: [22]

N-type:

$$\frac{1}{C_{SC}^2} = \frac{2}{\epsilon_r \epsilon_0 e N_D} \left(E - E_{FB} - \frac{kT}{q} \right) \quad (1)$$

P-type:

$$\frac{1}{C_{SC}^2} = \frac{-2}{\epsilon_r \epsilon_0 e N_A} \left(E - E_{FB} - \frac{kT}{q} \right) \quad (2)$$

where C_{SC} is the capacitance of space charge region, E is the applied potential (V_{SCE}), N_D and N_A represent the carrier concentration (cm^{-3}), e is the electron charge (1.602×10^{-19} C), ϵ_r is the dielectric constant of the passivation layer (oxide) (for a mixture of CoO and NiO $\epsilon_r = 10$ [23]), ϵ_0 is the vacuum dielectric constant (8.854×10^{-14} F cm^{-1}), T is the absolute temperature, k is the Boltzmann constant (8.16×10^{-5} eV/K), E_{FB} describes the flat band potential (V_{SCE}). Among the above parameters, C_{SC}^{-2} and N_D (N_A) are reciprocal.

In Figure 7(a) (b), the slope of the Mott-Schottky can determine the semiconductor type (N-type or P-type) on the surface of the sample, because the positive slope is N-type semiconductor and the negative slope is P-type semiconductor [24]. In Figure 7(a) (b), all plots obtained at 1kHz show positive slopes, indicating the formation of passivation/oxide layers with N-type semiconductor behavior on all samples studied in this paper. Due to the characteristics of N-type semiconductors, interstitial defects and oxygen vacancies are superior to cation vacancies in the passivation layer/oxide layer on the sample surface.

Figure 7(c) compares the calculated donor density of the passive film formed on different samples in 1.0 wt. % NaCl solution. It is found that the order of donor density measured at 1kHz is 16 h < 12 h < 20 h < 8 h (values are 2.77×10^{19} cm^{-3} , 1.33×10^{21} cm^{-3} , 5.16×10^{22} cm^{-3} and 6.29×10^{22} cm^{-3} respectively). The corrosion behavior of M-S is consistent with polarization curve and EIS. It is due to the tempering temperature changes the surface microstructure uniformity is reduced, the greater the donor density value represents the greater the internal defect density, at the same time because it is N-type semiconductor oxygen vacancy adsorption and penetration of corrosive substances and other factors. Considering the point defect model (PDM), the oxygen vacancy flux and interstitial defects (determined by their density and diffusivity) in the passivation film are the key factors controlling the growth and breakdown kinetics of the passivation film [25]. Therefore, the corrosion behavior shown by the M-S curve is consistent with the polarization and impedance curves. This further proves that the effect of tempering time on the corrosion behavior of the sample is related.

4. CONCLUSION

In this paper, through the analysis and discussion of the above results, the significant effect of tempering time on the microstructure and corrosion properties of high Co-Ni steel was revealed. The main conclusions are as follows:

(1) From the SEM, it can be seen that with the extension of tempering time, the martensite lath begins to grow and become longer, and finally the lath structure of martensite gradually disappears.

(2) The corrosion potential order of the samples is 16 h > 20 h > 12 h > 8 h. The polarization curves show that increasing the tempering time can make the corrosion potential move forward. The prolongation of tempering time effectively improves the overall stability of the sample surface and reduces the corrosion tendency of the sample. With the increase of tempering time, the corrosion current density of the sample decreases first and then increases ($I_{16h}=2.701\times 10^{-8} < I_{20h}=9.622\times 10^{-8} < I_{12h}=1.154\times 10^{-7} < I_{8h}=4.191\times 10^{-6}$). Considering the tempering time of 16h can effectively enhance the corrosion resistance of the sample.

(3) EIS results show that the sample austenitized at 950 °C for 1 h, then water quenched, cold treated at -73 °C for 1 h, and finally tempered at 482 °C for 16h has better corrosion resistance. Impedance fitting data and M-S curve can prove that the order of passivation layer thickness is 16 h > 20 h > 12 h > 8 h. At the same time, it can be judged by M-S that all curves obtained at 1kHz show a positive slope, indicating that a passivation/oxidation layer with N-type semiconductor behavior is formed on all samples studied in this paper.

ACKNOWLEDGMENT

The authors gratefully acknowledge the sponsorship from the National Natural Science Foundation of China (NO. 51574147 and NO. 52274062) and the Liaoning Provincial Natural Science Foundation of China (NO. 201602474).

References

1. A. S. Milani, and A. Shanian, *Int. J. Mech. Mater. Des.*, 3 (2006) 209.
2. S. Taktak, *Surf. Coat. Technol.*, 201 (2006) 2230.
3. C. Wang, C. Zhang, and Z. Yang, *J. Iron. Steel Res. Int.*, 24 (2017) 177.
4. C. Wang, C. Zhang, and Z. Yang, *Micron*, 67 (2014) 112.
5. W. J. Yang, M. Zhang, Y. H. Zhao, M. L. Shen, H. Lei, L. Xu, J. Q. Xiao, J. Gong, B. H. Yu, and C. Sun, *Surf. Coat. Technol.*, 298 (2016) 64.
6. S. Papula, S. Anttila, J. Talonen, T. Sarikka, I. Virkkunen, and Hannu Haenninen, *Mater. Sci. Eng. A*, 677 (2016) 11.
7. J. Park, and Y. Park, *Mater. Sci. Eng. A*, 449 (2007) 1131.
8. Abbasi-Khazaei Bijian, and Mollaahmadi Akbar, *J. Mater. Eng. Perform.*, 26 (2017) 1626.
9. Y. Zhao, W. Liu, Y. Fan, T. Zhang, B. Dong, L. Chen, and Y. Wang, *Mater. Charact.*, 175 (2021) 111066.
10. Rusnaldy, Efendi Mabruri, and Luky W. Nugroho, *IOP Conf. Ser.: Mater. Sci. Eng.*, 547 (2019) 012059.

11. K. H. Anantha, C. Ornek, S. Ejnermark, A. Medvedeva, J. Sjostrom, and J. Pan, *J. Electrochem. Soc.*, 164 (2017) C85.
12. L.C. Lim, M.O. Lai, and J. Ma, *Mater. Sci. Eng. A*, 171 (1993) 13.
13. F. Yuan, G. Wei, S. Gao, S. Lu, H. Liu, S. Li, X. Fang, and Y. Chen, *Corros. Sci.*, 203 (2022) 110346.
14. S. S. Wang, D. L. Peng, L. Chang, and X. D. Hui, *Mater. Des.*, 50 (2013) 174.
15. C. Pandey, and M. M. Mahapatra, *Process Mech. Eng.*, 231 (2017) 1141.
16. K. Zhang, X. Sun, Q. Yong, Z. Li, G. Yang, and Y. Li, *Acta Metall. Sin.*, 51 (2015) 553.
17. Joseph Raj Xavier, and Rajendran Nallaiyan, *J. Fail. Anal. Prev.*, 16 (2016) 1082.
18. X. Qi, H. Mao, and Y. Yang. *Corros. Sci.*, 120 (2017) 90.
19. Y. Lian, J. Zhang, P. Ji, Z. Zhang, M. Ma, C. Zhao, and J. Huang, *J. Mater. Eng. Perform.*, 31 (2022) 4963.
20. Y. Zhao, T. Zhang, H. Xiong, and F. Wang, *Corros. Sci.*, 191 (2021) 109763.
21. Y. Zhao, W. Qi, T. Zhang, H. Xiong and F. Wang, *Corros. Sci.*, 208 (2022) 110613.
22. A. G. Rao, V. A. Katkar, G. Gunasekaran, V. P. Deshmukh, N. Prabhu, and B. P. Kashyap, *Corros. Sci.*, 83 (2014) 198.
23. K. V. Rao, and A. Smakula, *J. Appl. Phys.*, 36 (1965) 2031.
24. G. A. Zhang, and Y. F. Cheng, *Electrochim. Acta*, 55 (2009) 316.
25. S. O. Gashti, and A. Fattah-alhosseini, *Anal. Bioanal. Electrochem.*, 6 (2014) 535.

© 2022 The Authors. Published by ESG (www.electrochemsci.org). This article is an open access article distributed under the terms and conditions of the Creative Commons Attribution license (<http://creativecommons.org/licenses/by/4.0/>).